Published in final edited form as:

J Am Chem Soc. 2024 July 24; 146(29): 19782–19791. doi:10.1021/jacs.4c02183.

Differential Lipid Binding Specificities of RAP1A and RAP1B are Encoded by the Amino Acid Sequence of the Membrane Anchors

Mussie K. Araya,
Department of Integrative Biology and Pharmacology, McGovern Medical School, University of Texas Health Science Center, Houston, Texas 77030, United States

Wei Chen,
Department of Integrative Biology and Pharmacology, McGovern Medical School, University of Texas Health Science Center, Houston, Texas 77030, United States

Yuepeng Ke,
Center for Translational Cancer Research, Institute of Biosciences and Technology, Texas A&M University, Houston, Texas 77030, United States; Department of Translational Medical Sciences, School of Medicine, Texas A&M University, Houston, Texas 77030, United States

Yubin Zhou,
Center for Translational Cancer Research, Institute of Biosciences and Technology, Texas A&M University, Houston, Texas 77030, United States; Department of Translational Medical Sciences, School of Medicine, Texas A&M University, Houston, Texas 77030, United States

Alemayehu A. Gorfe,
Department of Integrative Biology and Pharmacology, McGovern Medical School, University of Texas Health Science Center, Houston, Texas 77030, United States; Graduate School of Biological Sciences, M. D. Anderson Cancer Center and University of Texas Health Science Center, Houston, Texas 77030, United States

John F. Hancock,
Department of Integrative Biology and Pharmacology, McGovern Medical School, University of Texas Health Science Center, Houston, Texas 77030, United States; Graduate School of Biological Sciences, M. D. Anderson Cancer Center and University of Texas Health Science Center, Houston, Texas 77030, United States

Junchen Liu

Corresponding Author: Junchen Liu – Department of Integrative Biology and Pharmacology, McGovern Medical School, University of Texas Health Science Center, Houston, Texas 77030, United States; Graduate School of Biological Sciences, M. D. Anderson Cancer Center and University of Texas Health Science Center, Houston, Texas 77030, United States; junchen.liu@uth.tmc.edu.

Supporting Information

The Supporting Information is available free of charge at https://pubs.acs.org/doi/10.1021/jacs.4c02183.

EM evaluation of effector site mutants of RAP1A/B; protein levels of different RAP1 PBD mutants; gold labeling density and L_{max} values for each PBD mutant; confocal imaging of subcellular distribution of GFP-tagged RAP1A PBD mutants; and backbone and side-chain localization of selected RAP1A and 1B mutants (PDF)

Complete contact information is available at: https://pubs.acs.org/10.1021/jacs.4c02183

The authors declare no competing financial interest.

Department of Integrative Biology and Pharmacology, McGovern Medical School, University of Texas Health Science Center, Houston, Texas 77030, United States; Graduate School of Biological Sciences, M. D. Anderson Cancer Center and University of Texas Health Science Center, Houston, Texas 77030, United States

Abstract

RAP1 proteins belong to the RAS family of small GTPases that operate as molecular switches by cycling between GDP-bound inactive and GTP-bound active states. The C-terminal anchors of RAP1 proteins are known to direct membrane localization, but how these anchors organize RAP1 on the plasma membrane (PM) has not been investigated. Using high-resolution imaging, we show that RAP1A and RAP1B form spatially segregated nanoclusters on the inner leaflet of the PM, with further lateral segregation between GDP-bound and GTP-bound proteins. The C-terminal polybasic anchors of RAP1A and RAP1B differ in their amino acid sequences and exhibit different lipid binding specificities, which can be modified by single-point mutations in the respective polybasic domains (PBD). Molecular dynamics simulations reveal that single PBD mutations substantially reduce the interactions of the membrane anchors with the PM lipid phosphatidylserine. In summary, we show that aggregate lipid binding specificity encoded within the C-terminal anchor determines PM association and nanoclustering of RAP1A and RAP1B. Taken together with previous observations on RAC1 and KRAS, the study reveals that the PBD sequences of small GTPase membrane anchors can encode distinct lipid binding specificities that govern PM interactions.

Graphical Abstract

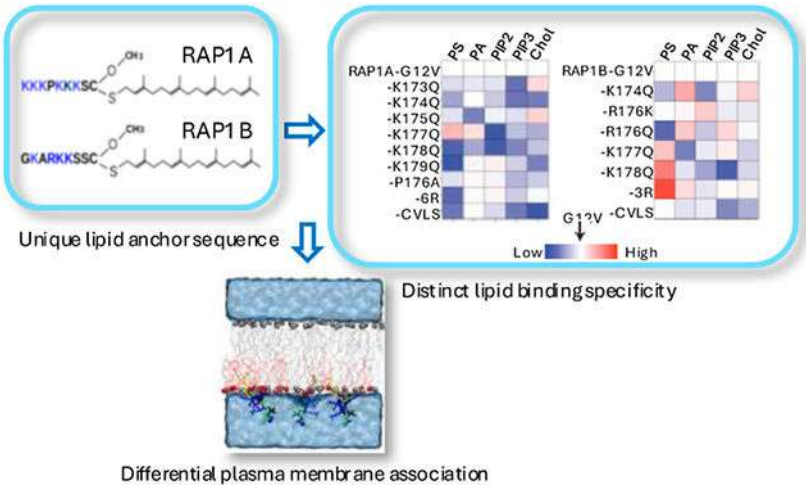

INTRODUCTION

RAP1 proteins operate as binary switches that oscillate between inactive GDP-bound and active GTP bound states to activate signaling cascades linked to wide-ranging cellular functions including cell–cell junctions, endothelial barrier functions, and immune activation.[1–5] RAP1 is activated by guanine nucleotide exchange factors (GEFs) including CalDAG-GEFI.[6] RAP1-GTP then interacts with downstream effectors including RIAM to

exert distinct cellular functions.[7] The conversion of RAP1-GTP to RAP1-GDP is facilitated by GTPase activating proteins that include RAPGAP.[8]

To function, RAP1 proteins must be localized to the plasma membrane (PM) via a C-terminal anchor containing a *S*-geranylgeranyl cysteine carboxymethyl ester and a polybasic domain [polybasic domains (PBD)]. Similar PBDs are found in other small GTPases including KRAS4B, RAC1, and CDC42. Distinct lipid binding specificities of KRAS and RAC1 are encoded by these PBD membrane anchors. For instance, the PBD anchor of KRAS specifically interacts with mixed acyl chain species of phosphatidylserine (POPS) (PS), whereas the RAC1 PBD anchor exhibits strong affinity for phosphatidic acid (PA) and phosphatidylinositol-trisphosphate (PIP_3).[9,10] The highly specific interactions between the C-terminal anchors and defined PM lipids result in the formation of nanoclusters. The nanoclusters typically comprise 6–7 molecules, possess a lifetime of a half second,[11–15] and undergo nucleotidedependent lateral segregation. These lipid-based nanoclusters are necessary for the activation of downstream signaling cascades.[16,17] For example, reducing the PM PS content has a profound effect on KRAS PM localization and function.[18,19] Likewise, depleting PM PA or PIP_3 mislocalizes RAC1 from the PM and impairs RAC1-dependent micropinocytosis.[10] It remains unclear whether similar mechanisms might also operate for RAP1 proteins and regulate their PM localization and hence function.

RAP1 isoforms are encoded by two different genes: RAP1A and RAP1B. The two isoforms share 95% sequence identity but exhibit distinct functions.[20] The sequence differences are confined to the C-terminus that includes the six residues that comprise the PBDs of the two proteins. In this study, we combine site-specific mutagenesis, electron microscopy, spatial mapping, and molecular simulations to show that RAP1 proteins assemble into nanoclusters with distinct lipid compositions. The formation of these nanoclusters is driven by interactions between specific amino acid residues within PBD anchors and defined PM lipids. RAP1A and RAP1B nanoclusters exhibit differential lipid binding preferences and sensitivities to point mutations within the PBD anchors, which are likely relevant to their isoform specific functions.

RESULTS

RAP1A and RAP1B Form Nanoclusters on the PM.

To determine the nanoscale organization of RAP1A and RAP1B on PM, we employed high-resolution spatial mapping. Intact PM sheets were prepared from baby hamster kidney (BHK) cells expressing green fluorescent protein (GFP)-tagged wild-type (WT), constitutively inactive GDP-bound (S17N), or constitutively active GTP-bound (G12V) RAP1A or RAP1B. The PM sheets were fixed and labeled with 4.5 nm gold conjugated anti-GFP antibodies and imaged by EM. The gold patterns were then analyzed using univariate K-functions expressed as $L(r) - r$. We use gold-labeling density (μm^{-2}) to quantify membrane recruitment and the maximum value of $L(r) - r$ ($=L_{max}$) to quantify the extent of clustering. The results showed that RAP1A and RAP1B form nanoclusters on the PM reflected by L_{max} values >1 (Figure 1A–G), mirroring RAC1 and KRAS nanoclusters.[10,21] Wild-type RAP1A (RAP1A-WT) and constitutively GDP-bound RAP1A (RAP1A-S17N) exhibited decreased PM binding compared with GTP-bound RAP1A

(RAP1A-G12V) (Figure 1C). Likewise, PM binding of GDP-bound RAP1B (RAP1B-S17N) was significantly lower than that of GTP bound-RAP1B (RAP1B-G12V), whereas wild-type RAP1B (RAP1B-WT) showed PM binding equivalent to that of RAP1B-GTP (Figure 1F). To test whether GTP-dependent PM localization is linked to effector binding, we generated D38A mutants which block effector interactions of RAP1A and RAP1B.[22] The D38A mutation significantly reduced the extent of PM localization and nanoclustering of both RAP1A and RAP1B (Figure S1A–D). These results show that PM localization of RAP1A and RAP1B is enhanced in the activated GTP-bound state as a result of effector-dependent interactions.

RAP1A and RAP1B Nanoclusters Spatially Segregate in a GTP-Dependent Manner.

Previous studies have shown that KRAS and RAC1 exhibit GTP-dependent segregation.[10,15,17] We therefore investigated whether this is the case for RAP1A and RAP1B by using bivariate EM spatial mapping. PM sheets from BHK cells coexpressing GFP-tagged RAP1-G12V and RFP-tagged RAP1-S17N were attached to the EM grids, fixed, and labeled with 6 and 2 nm gold particles conjugated with anti-GFP and anti-RFP antibodies, respectively. EM grids were then imaged, and gold particle distributions were analyzed using bivariate K functions [$L_{biv}(r) - r$] and L_{biv}-integrated (LBI) values as a summary statistic. LBI values positively correlate with the extent of coclustering, with LBI > 100 indicating significant coclustering of any two given gold populations. The high LBI values in control experiments indicate that GFP-RAP1A-G12V is significantly coclustered with RFP-RAP1A-G12V, and GFP-RAP1A-S17N is significantly coclustered with RFP-RAP1A-S17N (Figure 1H). In contrast, GFP-RAP1A-G12V and RFP-RAP1A-S17N exhibit a low LBI value, indicating spatial segregation between GDP and GTP bound RAP1A (Figure 1H). By similar reasoning, GFP-RAP1B-G12V coclustered with RFP-RAP1B-G12V, whereas RAP1B-WT colocalized with RAP1B-G12V, not RAP1B-S17N (Figure 1H). An LBI value just above the confidence interval (~100) indicates that RAP1B-G12V is minimally coclustered with RAP1B-S17N. Taken together, these data suggest that unlike RAP1A, wild-type RAP1B may be substantially GTP-loaded under serum replete conditions. In sum, these results indicate that both RAP1A and RAP1B undergo GTP-dependent lateral segregation to form spatially distinct GTP and GDP nanoclusters.

RAP1A and RAP1B Exhibit Distinct Lipid Specificities.

The C-terminal anchors of RAP1A and RAP1B comprise a geranylgeranylated CAAX motif and distinct adjacent PBDs (Figure 2D). We therefore examined the lipid specificities of each C-terminal anchor. PM sheets were prepared from BHK cells coexpressing RFP-RAP1A or RAP1B and a series of lipid probes for PS (GFP-LactC2),[23] PA (GFP-PASS),[24] phosphatidylinositol-bisphosphate (PIP_2) (GFP-PH-PLCδ),[25] PIP_3 (GFP-PH-AKT),[26] and cholesterol (GFP-D4H).[27] The PM sheets were then fixed and labeled with anti-GFP coupled to 6 nm gold and anti-RFP coupled to 2 nm gold, imaged by EM and analyzed using bivariate K-functions. RAP1A-G12V exhibited high LBI values with PS and PIP_3 probes and lower values with PIP2 and PA probes (Figure 2A), indicating nanoclusters enriched in PS and PIP_3 and to a lesser extent with PIP_2 and PA. Compared with RAP1A-WT, colocalization of RAP1A-GTP with PS, PIP_2, and PIP_3 was significantly enhanced. RAP1B-G12V and RAP1B-WT displayed high coclustering with cholesterol (GFP-D4H) and weak

colocalization with all other lipids tested (Figure 2B). These differing lipid binding profiles imply that RAP1A and RAP1B operate in spatially distinct nanoclusters on the PM, which have different lipid compositions. Concordantly, following the experimental spatial mapping approach of Figure 1, we indeed observe that GFP-RAP1A-G12V and RFP-RAP1B-G12V do not cocluster on the PM (Figure 1I).

Lipid Binding Specificities are Encoded in the Membrane Anchor of RAP1A and RAP1B.

Previous studies showed that the lipid binding specificity of the KRAS C-terminal anchor is encoded by the amino acid sequence of the PBD operating in concert with the prenyl group. To investigate whether this is also the case for RAP1A, we sequentially mutated each lysine to glutamine to generate RAP1A-G12V-K173Q, RAP1A-G12V-K174Q, RAP1A-G12V-K175Q, RAP1A-G12V-K177Q, RAP1A-G12V-K178Q, and RAP1A-G12V-K179Q (Figure 2C,) and repeated the lipid mapping experiments as described above. The heatmap summary of these data shows that despite possessing an equal net charge, each of these mutants exhibited distinct lipid binding specificities (Figure 2E). For example, nanoclusters of RAP1A-G12V-K173Q displayed a significant reduction in the PIP3 content, a modest albeit nonsignificant reduction in PS, PIP_2, and PA and a modest but nonsignificant enrichment with cholesterol compared to RAP1A-G12V (Figure 2E). RAP1A-G12V-K179Q nanoclusters exhibited yet a different lipid composition, with both PS and cholesterol significantly decreased compared to those of RAP1A-G12V (Figure 2E). We next replaced all six lysine residues with arginine to create a 6R-PBD mutant. Despite having an equal net charge, RAP1A-6R-G12V nanoclusters had a very different lipid composition to those of RAP1A-G12V (Figure 2E). An interesting feature of the RAP1A PBD is the presence of a proline residue that splits the polylysine sequence. To evaluate the impact of this proline on lipid sorting, we mutated it to alanine: RAP1A-G12V-P176A exhibited reduced PS and PIP_3 interactions compared with RAP1A-G12V. To evaluate if the type of prenylation affects lipid sorting specificity, we switched the CAAX motif from CLLL, which directs geranylgeranylation, to CVLS, which directs farnesylation. RAP1A-G12V-CVLS exhibited reduced binding to all lipids except PA, indicating a fundamentally different lipid binding specificity of the PBD in the context of a farnesylated C-terminal cysteine (Figure 2E).

The PBD of geranylgeranylated RAP1B anchor contains three lysines and one arginine (Figure 2D). Following a similar rationale to that for RAP1A, we conducted scanning mutagenesis and lipid mapping analysis. Single lysine or arginine to glutamine mutations generated RAP1B-G12V-K174Q, RAP1B-G12V-R176Q, RAP1B-G12V-K177Q, and RAP1B-G12V-K178Q (Figure 2D). The heatmap summary of these data in Figure 2F shows that each of these mutant anchors exhibited different lipid-binding specificities from the wild-type anchor. For example, PS and PIP_2 binding significantly decreased, and cholesterol and PA binding significantly increased when K174 was mutated to Q. In contrast, RAP1B-G12V-K178Q nanoclusters had a lower PIP_2 and PIP_3 content but a significant increase in the PS content. Replacing the three lysine residues with arginine resulted in nanoclusters with an enriched PS and PA content but a reduced PIP_2 content (Figure 2F). Replacing the geranylgeranyl anchor with farnesyl (RAP1B-G12V-CVLS) resulted in reduced interactions with all lipids except PS. These results show that lipid

sorting specificity is encoded by the precise PBD sequence and prenyl group that comprise the RAP1A and RAP1B anchors.

PM Localization of RAP1 is Determined by the Amino Acid Sequence of Membrane Anchor.

We next conducted a univariate EM analysis in BHK cells expressing each of the RAP1A and RAP1B PBD mutants. Despite comparable protein levels in whole cell lysates (Figure S1E), many mutants displayed altered PM binding and nanoclustering. We found that L_{max} and gold labeling density for RAP1A-G12V-K173Q, -K178Q, and -P176A were much lower than those for RAP1A-G12V (Figure 3A,B), indicating impaired nanoclustering and PM binding. Farnesylated RAP1A-G12V-CVLS also exhibited reduced PM binding and clustering. By contrast RAP1A-G12V-K179Q exhibited reduced PM localization but the protein that remained on the PM nanoclustered to the same extent as RAP1A-G12V. RAP1B-G12V-K174Q and RAP1B-K178Q exhibited reduced PM localization and clustering (Figure 3C) as did the phosphorylation mimicking mutant RAP1B-G12V-S179D (Figure 3C), suggesting a role of serine phosphorylation in regulating RAP1B PM binding. Farnesylated RAP1B-G12V-CVLS showed a reduced PM localization and nanoclustering (Figure 3C). Overall, gold labeling density and L_{max} values of each RAP1A PBD mutant are highly correlated (Figure S2A). For RAP1B mutants, most PBD mutants exhibit diminished clustering compared to RAP1B-G12V. An outlier is RAP1B-K178Q, which showed a greater reduction in L_{max}, suggesting that the mutation might affect the interaction of the C-terminal anchor with PM lipids primarily concerned with nanoclustering. Given that K178Q exhibited significantly less PIP3 association, we conclude that PIP_3 binding is likely required for the nanoclustering of RAP1B. Taking these results together with the lipid mapping analyses, we contend that the aggregate lipid binding specificity, encoded in the PBD-prenyl anchors of RAP1A and RAP1B, determines the extent of PM binding and nanoclustering.

Molecular Dynamics (MD) Simulations Reveal That Interaction of RAP1 Membrane Anchors with Anionic PS Lipid is Sequence Dependent.

To examine how mutation of specific Lys or Arg residues to Gln in the PBD may affect interactions with lipids, we conducted atomistic MD simulation of RAP1A-K173Q, RAP1A-K178Q, RAP1B-K174Q, and RAP1B-R176Q membrane anchors in a previously characterized asymmetric phosphatidylcholine (POPC)/POPS bilayer[28] (Figure 4A). These mutants were selected because they showed the largest impact on PM binding (Figure 3). Using the equilibrated portions of these trajectories (see Experimental Section), we analyzed the anchors in terms of their bilayer adsorption propensities and interactions with lipids and compared the results with data for wild-type RAP1A and RAP1B from recently reported simulations.[29] In all four simulations, the geranylgeranyl chain of the anchors is fully inserted into the core of the bilayer, while the backbone is adsorbed into the headgroup region (Figure 4B). Despite their overall flexibility, the anchors adopted a specific organization on the bilayer surface (Figure S3). The RAP1B anchors are largely extended and lie roughly flat on the bilayer surface, while those of RAP1A are curved with residues in the middle of the peptides remaining distal from the bilayer surface (Figure S3). In this regard, the mutant anchors share an overall similarity with their wild-type counterparts, but there are also notable differences. To examine these differences in detail,

we compared the time-averaged distributions of the number of hydrogen bonding (HB) (N_{HB}) and van der Waals contacts (N_C) between each anchor and the POPS and POPC lipids (Figure 5A). A major consequence of the mutations on both RAP1A and RAP1B anchors is a reduction in lipid selectivity, as can be seen from the smaller average N_{HB} per peptide with POPS [N_{HB}(PS)] in the mutants compared with the wild-type (Figure 5A). N_{HB}(PC) is slightly increased in the RAP1A mutants and decreased or unchanged in the RAP1B mutants. The mutations also have different effects on interactions of the anchors with lipid tails, as assessed by N_C (Figure 5A): relative to the wild-type anchors, N_C(PS) has slightly increased in RAP1A and decreased in RAP1B mutants while N_C(PC) is unchanged in the former and slightly increased in the later.

The effects of the mutations on HB and vdW interactions cannot be ascribed solely to the loss of a positive charge because the reduction in N_{HB}(PS) is greater than one, and the magnitude of the change is different between RAP1A-K173Q and RAP1A-K178Q as well as between RAP1B-K174Q and RAP1B-R176Q despite their equivalent net charge. For a closer examination of this issue, we calculated the frequency of hydrogen bond interactions of each Lys or Arg residue of the anchors with POPS headgroup oxygen atoms (Figure 5B). One can see that the mutations caused an overall reduction in HB with POPS, and that the effect is not limited to the mutated residue or its vicinity. Taken together, we find that a major impact of the selected PBD mutations to Gln was a reduction in the preference for PS lipids, consistent with our observation from the EM spatial mapping of RAP1A-G12V-K178Q (Figure 3C) and RAP1B-G12V-R176Q (Figure 3D).

Discussion.

Activation of RAP1 upon GTP binding promotes localization of RAP1 from perinuclear areas to the PM in human and Drosophila immune cells.[30,31] Our EM analysis is concordant with these observations in that GTP-bound RAP1A and RAP1B proteins exhibited increased PM association compared to that of the GDP-bound proteins. The subsequent lipid mapping analyses further extended these findings to specific nanodomains of PM with defined lipid compositions. RAP1A GTP nanoclusters showed enrichment with PS, PIP_2, and PIP_3 compared to wild-type RAP1A.GDP nanoclusters. We also observed that RAP1A PBD mutants, such as RAP1A-G12V-K173Q, RAP1A-G12V-K178Q, and RAP1A-G12V-CVLS, which exhibited defects in PS or PIP_3 binding, were depleted from the PM. Taken together, these results strongly suggest that interactions with PS and PIP_3 are essential for RAP1A.GTP PM interactions. In this context, it is interesting to note that CalDAG-GEFI, a GEF for RAP1, directly associates with PIP_2 and PIP_3 through its C1 domain,[32] and lipid binding domains for these same lipids are found in the RAP1 effector RIAM (RAP1-GTP interacting adaptor molecule).[33,34] A similar mode of action also operates for another RAP1 effector, talin, during integrin activation. PIP_2 and RAP1B synergistically recruit talin to the PM,[35,36] and the F1 domain and positively charged patches in F2 and F3 domains of talin also independently bind to PIP_2,[35] the same lipids that are found enriched in RAP1B nanoclusters here. Therefore, directly analogous to RAS nanoclusters,[16,18,19] the PM lipids recruited by RAP1A and RAP1B into nanoclusters generates lipid platforms which allows for efficient GEF and effector recruitment, and likely facilitates signaling propagation.

The backbone structure of wild-type RAP1A and RAP1B anchors observed during MD simulations suggests that RAP1B is more extended and more effectively adsorbs into our model membrane than RAP1A.[29] MD simulations also suggest that all basic residues of the Rap1B anchor, except K177, interact with the bilayer through high-frequency HBs with PS, whereas some basic residues in the RAP1A PBD engage PS at lower frequencies (Figure 5B). On average, however, interactions of wild-type Rap1A and RAP1B anchors with lipids through both HB and vdW contacts are similar (Figure 5A). By contrast, compared with RAP1A, mutations in Rap1B PBD resulted in a greater loss of HBs and vdW contacts with PS [smaller N_{HB}(PS) and N_C(PS) than the wild-type], coupled with an increase in N_C(PC). Therefore, PBD mutants that show reduced interaction with the head groups (N_{HB}) and acyl chains (N_C) of POPS seem to have greater effects on PM localization and nanoclustering in RAP1B than that in RAP1A. A key feature of the dynamic lipid anchors is that point mutations cause changes in conformational plasticity of the peptides such that their effect is not limited to the site of mutation alone but rather extends to the overall conformational ensembles sampled. It is their effect on the aggregate HBs and vdW contacts that modulates affinity for the PM. Therefore, the effect of the point mutations should be viewed beyond a direct side chain-lipid interaction but rather as an effect on the global structure and dynamics of the anchors.

Despite these differences, the PBD of RAP1A and RAP1B shows similar trends in PM and lipid binding. Specifically, we found that reduction of the net positive charge at the PBD by one through a single-point mutation of selected PBD residues resulted in a significant reduction in interactions with POPS lipids. However, the regulation of lipid specificity is beyond simple electrostatics. First, each K to Q, or R to Q mutant exhibited a different lipid composition from the wild-type and among the mutants. Despite altered lipid specificity, many arginine mutants including RAP1A.K174Q, RAP1A.K175Q, and RAP1B.K178Q maintained PM association, suggesting that each lysine is nonequivalent in determining PM targeting. Furthermore, RAP1 anchor mutants that replace all lysine residues with arginine (RAP1A-G12V-6R and RAP1B-G12V-3R) exhibited distinct lipid sorting from that of RAP1-G12V with a wild-type PBD. Moreover, replacing the geranylgeranyl group with the farnesyl group that contains shorter alkyl chains (CVLS mutants) again generates nanoclusters with strikingly different lipid compositions. These mutants also displayed impaired PM association compared with RAP1 with wild-type anchors, which is likely attributed to decreased hydrophobicity by switching from 20-carbon geranylgeranyl to 15-carbon farnesyl groups. We concluded that PM binding and nanoclustering of RAP1 proteins are likely determined by the aggregate lipid specificity that is encoded in the geranylgeranylpolybasic membrane anchors. The observation extends our previous observations in KRAS and RAC1[10,21] to small GTPases with similar C-terminal polybasic anchors, revealing a universal principle that localizes these proteins to the PM, and possibly other intracellular lipid bilayers. Effector site mutants RAP1A/B-G12V-D38A exhibited reduced PM association, mirroring the distribution pattern of GDP-bound RAP1. These results have shown that the PM localization of activated GTP-bound RAP1A and B is enhanced by binding to cognate effectors. Interestingly, this recalls previous results with RAB proteins including RAB6 where it was first shown that the anchor and effector domains cooperate for correct subcellular localization.[37] As discussed above, the spatial organization

of small GTPases on the PM is driven by interactions between lipid-modified HVR anchors and phospholipids at the PM, with G-domains playing no direct roles.[15] In the context of the extensive literature on KRAS, we propose that while binding to effectors increases the PM abundance of GTP-loaded RAP1, such interactions are unlikely to regulate the lateral segregation of RAP1 isoforms, which is determined by specific HVR sequence that encodes unique lipid binding specificities. Further studies will be required, however, to formally demonstrate this proposition.

PM localization of small GTPases may involve PDEδ, a cytosolic chaperone that solubilizes the small GTPase after internalization from the PM and returns it back to the PM through a complex mechanism that involves vesicular trafficking by the recycling endosome.[38–40] Structural analyses show that for geranylgeranylated GTPases, the hydrophobic pocket within the immunoglobulin-like β-sandwich fold of PDEδ fully accommodates the prenylated cysteine but then only interacts with the four adjacent amino acids of the HVR. Therefore, the amino residues that interact with PDEδ are Lys^{178}-Lys^{179}-Ser^{180}-Cys^{181} for RAP1A and Lys^{178}-Ser^{179}-Ser^{180}-Cys^{181} for RAP1B. In this context, replacing a lysine with the marginally smaller amino acid glutamine (RAP1A-K178Q and -K179Q) greatly reduced PM abundance of RAP1A, even though the Glu would be readily accommodated in the Lys pocket, conversely replacing the lysines with much larger amino acid, arginines (RAP1A-6R), that would not be readily accommodated in the lysine pocket and hence would be expected to disrupt PDEδ binding that had no effect on RAP1A PM localization. These considerations imply that there is no correlation between PDEδ binding and the anchor mutations that can account for changes in the RAP1A PM interactions. Concordantly, the confocal imaging analysis did not reveal significant colocalization between each RAP1 mutant and PDEδ (Figure S2B). Together, these results and known structural biology of PDEδ argue against a model in which PM loss of RAP1A/B mutants is caused by impaired PDEδ binding. However, we cannot rule out the possibility that unknown chaperons might regulate the PM trafficking of RAP1, and that interactions with such proteins could be impacted by the HVR mutations.

These findings are likely relevant to previous observations that RAP1A and RAP1B play distinct roles in tissue-specific contexts and even in the same cells. For instance, RAP1A, but not RAP1B, is the primary isoform that localizes to and regulates endothelial cell junctions.[20] The relative contribution of each isoform to the EC junctions might be explained by the specific lipid composition at the junctions. In this context, cholesterol, which we have shown to be significantly enriched in RAP1A clusters, has been implicated in the regulation of cell–cell adhesion.[41]

CONCLUSIONS

In conclusion, this study reveals that the C-terminal anchors of RAP1 proteins, which direct membrane localization, play a critical role in organizing RAP1 on the PM. High-resolution imaging demonstrates that RAP1A and RAP1B form distinct nanoclusters on the inner leaflet of the PM, with GDP-bound and GTP-bound proteins showing further lateral segregation. PM localization of RAP1 is enhanced by effector binding such that GTP-bound RAP1A and 1B are significantly enriched on the PM compared to the GDP-bound

proteins. The C-terminal polybasic anchors of RAP1A and RAP1B, differing in amino acid sequence, exhibit unique lipid binding specificities. These specificities can be altered by single- or multiple-point mutations in the PBD. MD simulations indicate that these single PBD mutations significantly diminish interactions between the membrane anchors and the PM lipid POPS. Therefore, the lipid binding specificity encoded within the C-terminal anchor determines the PM association and nanoclustering of RAP1A and RAP1B. This study, in conjunction with previous findings on RAC1 and KRAS, further advances the premise that the primary PBD sequences of small GTPase membrane anchors encode distinct lipid binding specificities that dictate PM interactions. These in turn, may account for the isoform-specific functions of RAP1A and RAP1B.

EXPERIMENTAL SECTION

Plasmids.

Wild-type and G12V RAP1A and RAP1B plasmids were gifted by Dr. Mark Philips at NYU. Single-site and multiple-site RAP1 PBD mutants were designed with the QuikChange Prime Web site of Agilent. The PBD mutant constructs were generated using a QuikChange site-directed mutagenesis kit (# 200517) by Agilent. GFP-LactC2 was provided by Sergio Grinstein (The Hospital for Sick Children, Toronto, Canada). GFP-PASS, GFP-PH-AKT, and GFP-PLCδ were provided by Guangwei Du at the University of Texas Health Science Center, Houston, Texas.

Cell Culture and Transfection.

BHK cells were purchased from ATCC and routinely tested for the mycoplasma. The cells were cultured in DMEM medium containing 10% bovine calf serum and maintained in 37 °C 5% CO_2 humidified incubators. For cell transfection, BHK cells were seeded at 70% confluence on day 1. The next day, BHK cells were transfected with constructs for RAP1 or lipid probes using lipofectamine. On day 3, PM sheets of transfected BHK cells were fixed for subsequent EM analyses.

Transmission Electron Microscopy.

For univariate analyses, apical and lateral PM sheets of BHK cells were prepared and fixed with 4% PFA and 0.1% glutaraldehyde and labeled with anti-GFP antibodies conjugated with 4.5 nm gold or RFP antibodies conjugated with 2 nm gold. Images were then taken using a JEOL JEM-1400 transmission EM at 100,000× magnification. Image J was used to process the images and to assign x and y coordinates to gold particles in a 1 μm^2 area of interest on a PM sheet. Ripley's K-function was used to quantify the spatial distribution of gold particles under the null hypothesis that all gold points distribute randomly (A and B).

$$K(r) = An^{-2} \sum_{i \neq j} w_{ij} 1\left(\|x_i - x_j\| \leq r\right) \tag{A}$$

$$L(r) - r = \sqrt{\frac{K(r)}{\pi}} - r \tag{B}$$

where $K(r)$ = the univariate K-function for a pattern of n points in a selected PM area of A; r = length scale with the range of $1 < r < 240$ nm evaluated at increments of 1 nm; $\|\cdot\|$ is the Euclidean distance; $1(\cdot)$ is the indicator function with a value of 1 if $\|x_i - x_j\| \leq r$, and a value of 0 otherwise; and w_{ij}^{-1} is the fraction of the circumference of a circle with center x_i and radius $\|x_i - x_j\|$ contained within area A, rendering an unbiased edge correction for points at the edge of the study area. $K(r)$ is transformed into $L(r) - r$, which is then normalized on the 99% confidence interval (99% C.I.) estimated via Monte Carlo simulations. Under the null hypothesis of complete spatial randomness, $L(r) - r = 0$ for all values of r. Values of $L(r) - r$ exceeding the confidence interval indicates significant clustering at that value of r. The maximum value of the $L(r) - r$ function, ($L_{\max}$) is an unbiased summary parameter that can be used to quantify the extent of clustering.[12] At least 12 PM sheets were imaged, analyzed, and pooled. To evaluate the differences between replicated point patterns, a Bootstrap test was employed as described in C

$$D = \sum_{i=1}^{g} \int_{10}^{110} w(r) n_i [K_i(r) - K(r)]^2 \mathrm{d}r \tag{C}$$

where $w(r) = r^{-2}$, $K_i(r)$ = weighted mean K-function of the ith group of size n_i, and $K(r)$ = combined weighted mean K-function of all the groups being compared (g). The observed value of D was ranked against 1000 Monte Carlo simulated values of D calculated using a set of residual K-functions derived from each $K_i(r)$,[12,42] the rank is an estimate of the probability that the null hypothesis of equivalence can be rejected.

For bivariate analyses, PM sheets of BHK cells stably expressing GFP-tagged lipid probes and RFP-tagged RAP1 constructs were fixed and stained sequentially with anti-GFP 6 nm gold and ant-RFP 2 nm gold conjugated antibodies before being imaged and analyzed. Gold particles and colocalizations were calculated with bivariate K-functions (eqs D–G)

$$K_{\mathrm{biv}}(r) = (n_{\mathrm{b}} + n_{\mathrm{s}})^{-1} [n_{\mathrm{b}} K_{\mathrm{sb}}(r) + n_{\mathrm{s}} K_{\mathrm{bs}}(r)] \tag{D}$$

$$K_{\mathrm{bs}}(r) = \frac{A}{n_{\mathrm{b}} n_{\mathrm{s}}} \sum_{i=1}^{n_{\mathrm{b}}} \sum_{j=1}^{n_{\mathrm{s}}} w_{ij} 1\left(\|x_i - x_j\| \leq r\right) \tag{E}$$

$$K_{sb}(r) = \frac{A}{n_b n_s} \sum_{i=1}^{n_s} \sum_{j=1}^{n_b} w_{ij} 1\left(\|x_i - x_j\| \le r\right) \quad \text{(F)}$$

$$L_{biv}(r) - r = \sqrt{\frac{K_{biv}(r)}{\pi}} - r \quad \text{(G)}$$

where $K_{biv}(r)$ is the weighted mean of two individual bivariate K-functions with $K_{bs}(r)$ which evaluates the spatial distribution of big gold particles relative to each small gold particle and $K_{sb}(r)$ which evaluates the spatial distribution of small gold particles relative to each big gold particle. $K_{biv}(r)$ is transformed to $L_{biv}(r) - r$ and normalized to the 95% confidence interval (95% C.I.) estimated under Monte Carlo simulations. Under the null hypothesis, $L_{biv}(r) - r = 0$ at all values of r indicates no spatial interactions between two gold populations. Positive deviation of the $L_{biv}(r) - r$ exceeding the confidence interval indicates significant colocalizations of two gold patterns at that value of r. To quantify the extent of coclustering, area-under-the-$L_{biv}(r) - r$ curve over a defined scale length ($10 < r < 110$ nm) was calculated using the following equation and was termed as $L_{biv}(r) - r$ integrated or LBI (H)

$$LBI = \int_{10}^{110} \mathrm{Std} L_{biv}(r) - r \mathrm{d}r \quad \text{(H)}$$

At least 15 PM sheets were imaged, analyzed, and pooled. LBI values ≥100 indicate significant coclustering of the two gold patterns, and LBI <100 indicates no coclustering of the two-point patterns. Although the pooled LBI data are shown as mean ± SEM, the LBI parameter is not normally distributed. Therefore, statistical differences between the replicated bivariate-point patterns were evaluated by the same Bootstrap test described above (C).

MD Simulations.

We conducted MD simulations on RAP1A-K173Q, RAP1A-K178Q, RAP1B-K174Q, and RAP1B-R176Q in an asymmetric bilayer of POPC and POPS lipids. The protocols for system construction, simulation setup and execution, and trajectory analysis were the same as described recently for the simulation of RAP1A-WT and RAP1B-WT. Briefly, we mutated the relevant Lys or Arg residue on previously geranylgeranylated and oxo-methylated peptide structures to Gln using VMD[43] (see Figure 4A). We then attached three copies of each mutant peptide to the POPS-containing monolayer of a preequilibrated and TIP3P-solvated bilayer, as described previously.[28,29] The resulting 61,000–64,000 atom systems, exemplified in Figure 4B, were equilibrated as described previously[29] and simulated for 5 μs each on Anton 2, with trajectory frames saved every 100 ps for analysis.

Evaluation of time-dependent structural properties such as membrane thickness, root-mean-square derivation, and bilayer adsorption of the peptides showed that each system is fully stabilized within 2.5 μs. We therefore used the second half of each simulation for the analysis of equilibrium properties of the peptide-bilayer complex, with emphasis on peptide–lipid interactions assessed by the average numbers of hydrogen bond (N_{HB}) and vdW (N_C) contacts or residue-POPS HB frequencies (Figure 5). The results were then compared with data for the wild-type RAP1A and RAP1B membrane anchors from previous simulations,[29] using the same 2.5–5 μs trajectory segment as in the current analysis.

Supplementary Material

Refer to Web version on PubMed Central for supplementary material.

ACKNOWLEDGMENTS

This work was supported by a NIH grant (R01 GM124233), awarded to J.F.H. and A.A.G., a NIH grant (R01 GM144836) awarded to A.A.G., and a NIH grant (R01GM144986) and a Welch Foundation grant (BE-1913-20220331) awarded to Y.Z. Computational resources have been provided by the Texas Advanced Computing Center (TACC) and Anton 2. Anton 2 computer time was provided by the Pittsburgh Supercomputing Center (PSC) through grant R01GM116961 from the National Institutes of Health. The Anton 2 machine at PSC was generously made available by D.E. Shaw Research.

REFERENCES

(1). Arthur WT; Quilliam LA; Cooper JA Rap1 promotes cell spreading by localizing Rac guanine nucleotide exchange factors. J. Cell Biol 2004, 167, 111–122. [PubMed: 15479739]

(2). Tsukamoto N; Hattori M; Yang H; Bos JL; Minato N Rap1 GTPase-activating protein SPA-1 negatively regulates cell adhesion. J. Biol. Chem 1999, 274, 18463–18469. [PubMed: 10373454]

(3). Takahashi M; Dillon TJ; Liu C; Kariya Y; Wang Z; Stork PJ Protein kinase A-dependent phosphorylation of Rap1 regulates its membrane localization and cell migration. J. Biol. Chem 2013, 288, 27712–27723. [PubMed: 23946483]

(4). Chrzanowska-Wodnicka M; Smyth SS; Schoenwaelder SM; Fischer TH; White GC, 2nd Rap1b is required for normal platelet function and hemostasis in mice. J. Clin. Invest 2005, 115, 680–687. [PubMed: 15696195]

(5). Shah S; Brock EJ; Ji K; Mattingly RR Ras and Rap1: A tale of two GTPases. Semin. Cancer Biol 2019, 54, 29–39. [PubMed: 29621614]

(6). Crittenden JR; Bergmeier W; Zhang Y; Piffath CL; Liang Y; Wagner DD; Housman DE; Graybiel AM CalDAG-GEFI integrates signaling for platelet aggregation and thrombus formation. Nat. Med 2004, 10, 982–986. [PubMed: 15334074]

(7). Lafuente EM; van Puijenbroek AA; Krause M; Carman CV; Freeman GJ; Berezovskaya A; Constantine E; Springer TA; Gertler FB; Boussiotis VA RIAM, an Ena/VASP and Profilin ligand, interacts with Rap1-GTP and mediates Rap1-induced adhesion. Dev. Cell 2004, 7, 585–595. [PubMed: 15469846]

(8). Chen F; Barkett M; Ram KT; Quintanilla A; Hariharan IK Biological characterization of Drosophila Rapgap1, a GTPase activating protein for Rap1. Proc. Natl. Acad. Sci. U.S.A 1997, 94, 12485–12490. [PubMed: 9356476]

(9). Remorino A; De Beco S; Cayrac F; Di Federico F; Cornilleau G; Gautreau A; Parrini MC; Masson JB; Dahan M; Coppey M Gradients of Rac1 Nanoclusters Support Spatial Patterns of Rac1 Signaling. Cell Rep 2017, 21, 1922–1935. [PubMed: 29141223]

(10). Maxwell KN; Zhou Y; Hancock JF Rac1 Nanoscale Organization on the Plasma Membrane Is Driven by Lipid Binding Specificity Encoded in the Membrane Anchor. Mol. Cell. Biol 2018, 38, No. e00186. [PubMed: 29967243]

(11). Murakoshi H; Iino R; Kobayashi T; Fujiwara T; Ohshima C; Yoshimura A; Kusumi A Single-molecule imaging analysis of Ras activation in living cells. Proc. Natl. Acad. Sci. U.S.A 2004, 101, 7317–7322. [PubMed: 15123831]

(12). Plowman SJ; Muncke C; Parton RG; Hancock JF H-ras, K-ras, and inner plasma membrane raft proteins operate in nanoclusters with differential dependence on the actin cytoskeleton. Proc. Natl. Acad. Sci. U.S.A 2005, 102, 15500–15505. [PubMed: 16223883]

(13). Zhou Y; Prakash P; Gorfe AA; Hancock JF Ras and the Plasma Membrane: A Complicated Relationship. Cold Spring Harbor Perspect. Med 2018, 8, a031831.

(14). Sarkar-Banerjee S; Sayyed-Ahmad A; Prakash P; Cho KJ; Waxham MN; Hancock JF; Gorfe AA Spatiotemporal Analysis of K-Ras Plasma Membrane Interactions Reveals Multiple High Order Homo-oligomeric Complexes. J. Am. Chem. Soc 2017, 139, 13466–13475. [PubMed: 28863262]

(15). Simanshu DK; Philips MR; Hancock JF Consensus on the RAS dimerization hypothesis: Strong evidence for lipid-mediated clustering but not for G-domain-mediated interactions. Mol. Cell 2023, 83, 1210–1215. [PubMed: 36990093]

(16). Harding AS; Hancock JF Using plasma membrane nanoclusters to build better signaling circuits. Trends Cell Biol 2008, 18, 364–371. [PubMed: 18620858]

(17). Tian T; Harding A; Inder K; Plowman S; Parton RG; Hancock JF Plasma membrane nanoswitches generate high-fidelity Ras signal transduction. Nat. Cell Biol 2007, 9, 905–914. [PubMed: 17618274]

(18). Kholodenko BN; Hancock JF; Kolch W Signalling ballet in space and time. Nat. Rev. Mol. Cell Biol 2010, 11, 414–426. [PubMed: 20495582]

(19). Plowman SJ; Ariotti N; Goodall A; Parton RG; Hancock JF Electrostatic interactions positively regulate K-Ras nanocluster formation and function. Mol. Cell. Biol 2008, 28, 4377–4385. [PubMed: 18458061]

(20). Wittchen ES; Aghajanian A; Burridge K Isoform-specific differences between Rap1A and Rap1B GTPases in the formation of endothelial cell junctions. Small GTPases 2011, 2, 65–76. [PubMed: 21776404]

(21). Prior IA; Muncke C; Parton RG; Hancock JF Direct visualization of Ras proteins in spatially distinct cell surface microdomains. J. Cell Biol 2003, 160, 165–170. [PubMed: 12527752]

(22). Herrmann C; Horn G; Spaargaren M; Wittinghofer A Differential interaction of the ras family GTP-binding proteins H-Ras, Rap1A, and R-Ras with the putative effector molecules Raf kinase and Ral-guanine nucleotide exchange factor. J. Biol. Chem 1996, 271, 6794–6800. [PubMed: 8636102]

(23). Yeung T; Gilbert GE; Shi J; Silvius J; Kapus A; Grinstein S Membrane phosphatidylserine regulates surface charge and protein localization. Science 2008, 319, 210–213. [PubMed: 18187657]

(24). Lu M; Tay LW; He J; Du G Monitoring Phosphatidic Acid Signaling in Breast Cancer Cells Using Genetically Encoded Biosensors. Methods Mol. Biol 2016, 1406, 225–237. [PubMed: 26820960]

(25). Garcia P; Gupta R; Shah S; Morris AJ; Rudge SA; Scarlata S; Petrova V; McLaughlin S; Rebecchi MJ The pleckstrin homology domain of phospholipase C-.delta.1 binds with high affinity to phosphatidylinositol 4,5-bisphosphate in bilayer membranes. Biochemistry 1995, 34, 16228–16234. [PubMed: 8519781]

(26). Gassama-Diagne A; Yu W; ter Beest M; Martin-Belmonte F; Kierbel A; Engel J; Mostov K Phosphatidylinositol-3,4,5-trisphosphate regulates the formation of the basolateral plasma membrane in epithelial cells. Nat. Cell Biol 2006, 8, 963–970. [PubMed: 16921364]

(27). Maekawa M Domain 4 (D4) of Perfringolysin O to Visualize Cholesterol in Cellular Membranes-The Update. Sensors 2017, 17, 504. [PubMed: 28273804]

(28). Araya MK; Gorfe AA Phosphatidylserine and Phosphatidylethanolamine Asymmetry Have a Negligible Effect on the Global Structure, Dynamics, and Interactions of the KRAS Lipid Anchor. J. Phys. Chem. B 2022, 126, 4491–4500. [PubMed: 35687481]

(29). Araya MK; Gorfe AA Conformational ensemble-dependent lipid recognition and segregation by prenylated intrinsically disordered regions in small GTPases. Commun. Biol 2023, 6, 1111. [PubMed: 37919400]

(30). Siekhaus D; Haesemeyer M; Moffitt O; Lehmann R RhoL controls invasion and Rap1 localization during immune cell transmigration in Drosophila. Nat. Cell Biol 2010, 12, 605–610. [PubMed: 20495554]

(31). Bivona TG; Wiener HH; Ahearn IM; Silletti J; Chiu VK; Philips MR Rap1 up-regulation and activation on plasma membrane regulates T cell adhesion. J. Cell Biol 2004, 164, 461–470. [PubMed: 14757755]

(32). Sarker M; Goliaei A; Golesi F; Poggi M; Cook AA; Khan MA; Temple BR; Stefanini L; Canault M; Bergmeier W; et al. Subcellular localization of Rap1 GTPase activator CalDAG-GEFI is orchestrated by interaction of its atypical C1 domain with membrane phosphoinositides. J. Thromb. Haemostasis 2020, 18, 693–705. [PubMed: 31758832]

(33). Sun H; Lagarrigue F; Ginsberg MH The Connection Between Rap1 and Talin1 in the Activation of Integrins in Blood Cells. Front. Cell Dev. Biol 2022, 10, 908622. [PubMed: 35721481]

(34). Wynne JP; Wu J; Su W; Mor A; Patsoukis N; Boussiotis VA; Hubbard SR; Philips MR Rap1-interacting adapter molecule (RIAM) associates with the plasma membrane via a proximity detector. J. Cell Biol 2012, 199, 317–329. [PubMed: 23045549]

(35). Bromberger T; Zhu L; Klapproth S; Qin J; Moser M Rap1 and membrane lipids cooperatively recruit talin to trigger integrin activation. J. Cell Sci 2019, 132, jcs235531.

(36). Zhu L; Yang J; Bromberger T; Holly A; Lu F; Liu H; Sun K; Klapproth S; Hirbawi J; Byzova TV; et al. Structure of Rap1b bound to talin reveals a pathway for triggering integrin activation. Nat. Commun 2017, 8, 1744. [PubMed: 29170462]

(37). Beranger F; Paterson H; Powers S; de Gunzburg J; Hancock JF The effector domain of Rab6, plus a highly hydrophobic C terminus, is required for Golgi apparatus localization. Mol. Cell. Biol 1994, 14, 744–758. [PubMed: 8264642]

(38). Yelland T; Garcia E; Parry C; Kowalczyk D; Wojnowska M; Gohlke A; Zalar M; Cameron K; Goodwin G; Yu Q; et al. Stabilization of the RAS:PDE6D Complex Is a Novel Strategy to Inhibit RAS Signaling. J. Med. Chem 2022, 65, 1898–1914. [PubMed: 35104933]

(39). Dharmaiah S; Bindu L; Tran TH; Gillette WK; Frank PH; Ghirlando R; Nissley DV; Esposito D; McCormick F; Stephen AG; et al. Structural basis of recognition of farnesylated and methylated KRAS4b by PDEδ. Proc. Natl. Acad. Sci. U.S.A 2016, 113, E6766–E6775. [PubMed: 27791178]

(40). Chandra A; Grecco HE; Pisupati V; Perera D; Cassidy L; Skoulidis F; Ismail SA; Hedberg C; Hanzal-Bayer M; Venkitaraman AR; et al. The GDI-like solubilizing factor PDEδ sustains the spatial organization and signalling of Ras family proteins. Nat. Cell Biol 2012, 14, 148–158.

(41). Norman LL; Oetama RJ; Dembo M; Byfield F; Hammer DA; Levitan I; Aranda-Espinoza H Modification of Cellular Cholesterol Content Affects Traction Force, Adhesion and Cell Spreading. Cell. Mol. Bioeng 2010, 3, 151–162. [PubMed: 21461187]

(42). Diggle PJ; Mateu J; Clough HE A comparison between parametric and non-parametric approaches to the analysis of replicated spatial point patterns. Adv. Appl. Probab 2000, 32 (2), 331–343.

(43). Humphrey W; Dalke A; Schulten K VMD: visual molecular dynamics. J. Mol. Graphics 1996, 14, 33–38.

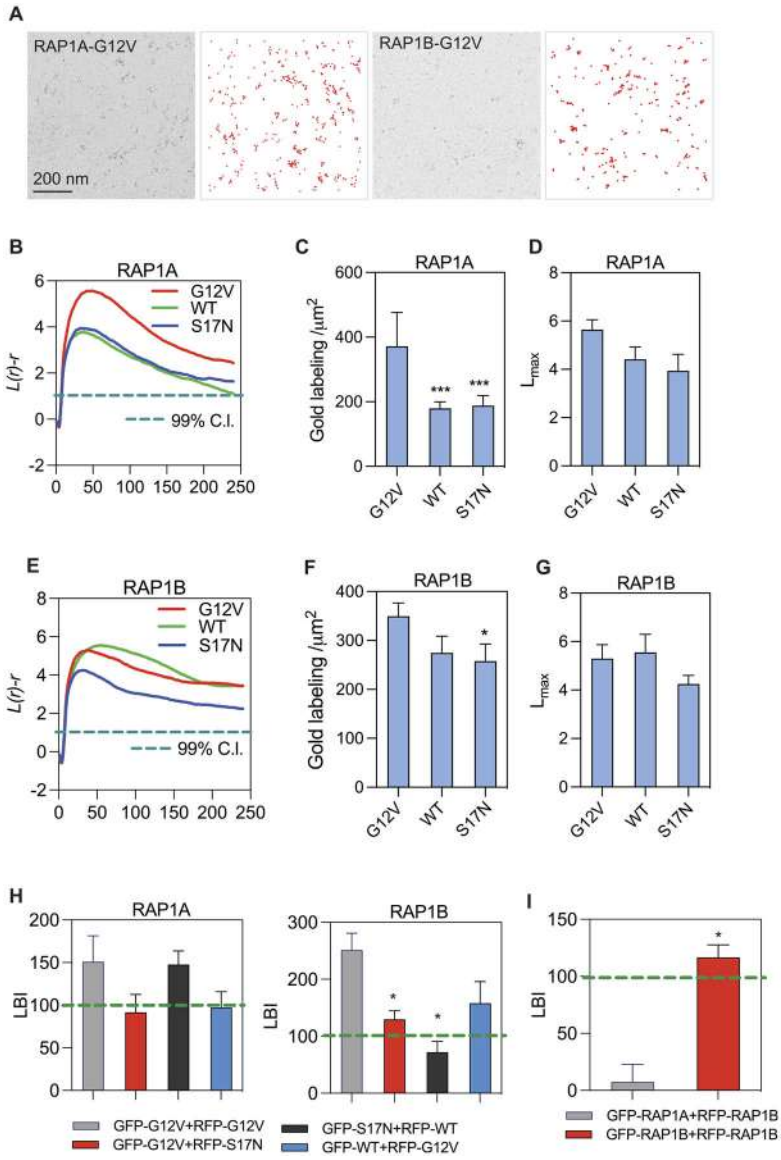

Figure 1.

RAP1A and RAP1B proteins form PM nanoclusters. (A) Representative EM images (1 μm^2) of 4.5 nm gold particles coupled to anti-GFP antibodies on PM sheets. Intact PM sheets were prepared from BHK cells expressing GFP-RAP1A-G12V or GFP-RAP1B-G12V and labeled with 4.5 nm gold-anti-GFP. Coordinates of each gold particle were used to generate digitalized images of the gold point patterns that are color-coded in red. (B–D) PM sheets of BHK cells expressing GFP-RAP1A-G12V, -wild-type (WT) or S17N were immunogold labeled and imaged by EM. Univariate K-functions were used to analyze the gold patterns. (B) Plots of weighted mean standardized univariate K-function are shown. Values of $L(r) - r$ above the 99% confidence interval (C.I) indicate significant clustering. (C) PM binding of GFP-RAP1A-G12V, -WT or S17N was quantified as mean gold labeling intensity (±SEM; (n = 12–17) for each condition). Student t tests were used to evaluate statistical differences between mean gold labeling density of GFP-RAP1A-G12V and GFP-RAP1A-WT or S17N

(***$p < 0.001$). (D) Peak value of $L(r) - r$ (=L_{max}) was used to summarize the extent of nanoclustering. L_{max} values are means ± SEM ($n = 10–15$). The significance of differences from control L_{max} values were analyzed using bootstrap tests. (E–G) The EM experiments in (B–C) were repeated in BHK cells expressing GFP-RAP1B-G12V, -WT or S17N ($n = 16–27$). Weighted mean univariate K-functions (E), mean gold labeling densities (F) and L_{max} values (G) for GFP-RAP1B-G12V, -WT or S17N are shown. (H) PM sheets from BHK cells coexpressing GFP- and RFP-RAP1A/B constructs were labeled with 6 nm gold-anti-GFP and 2 nm gold-anti-RFP and visualized by EM. Colocalization of GFP- and RFP-RAP1 proteins were analyzed by integrated bivariate K-functions (=LBI). The green dotted lines indicate 95% C.I. LBI values above the C.I (>100) indicate significant coclustering (±SEM; ($n \geq 12$) for each condition). (I) The bivariate EM experiment in (H) was repeated in BHK cells coexpressing GFP-RAP1A and RFP-RAP1B, or GFP-RAP1B and RFP-RAP1B. LBI values are means +SEM [($n = 10–14$) for each condition]. Bootstrap tests were used to evaluate the significance of statistical differences (*$p < 0.05$).

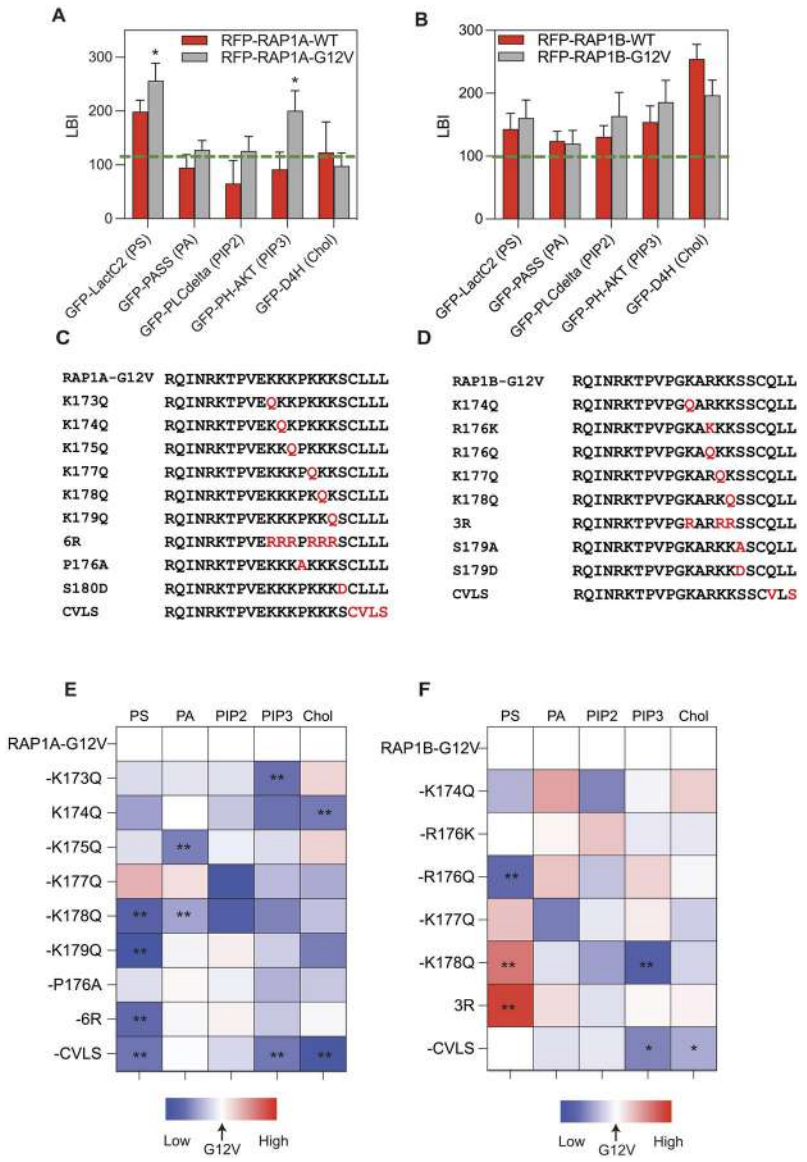

Figure 2.

Differential lipid sorting specificities are encoded in the membrane anchors of RAP1 proteins. (A,B) PM sheets of BHK cells coexpressing RFP-tagged wild-type (RFP-RAP1-WT) or GTP-bound mutant RAP1 (RFP-RAP1-G12V) with a GFP-tagged lipid probe for PS (GFP-LactC2), PIP2 (GFP-PLCδ), PIP3 (GFP-AKT), PA (GFP-PASS), or cholesterol (GFP-D4H) were labeled with 6 nm gold-anti-GFP and 2 nm gold-anti-RFP and imaged by EM. Bivariate coclustering analysis of the two gold populations yields LBI values [±SEM, ($n \geq 12$) for each condition] which reflect the lipid binding preferences of RAP1A (A) or RAP1B (B). (C,D) Details of mutations made in the RAP1A and RAP1B membrane anchor domains. (E,F) Heatmaps were generated using mean LBI values to quantify coclustering between each RFP-PBD mutant and each GFP-lipid probe. For each lipid probe, the LBI value for wild-type anchor construct (RAP1-G12V) was assigned as midpoint (marked in

white) with lower or higher LBI values marked in blue or red, respectively. Bootstrap tests were used to evaluate the significance of statistical differences (*$p < 0.05$, and **$p < 0.01$).

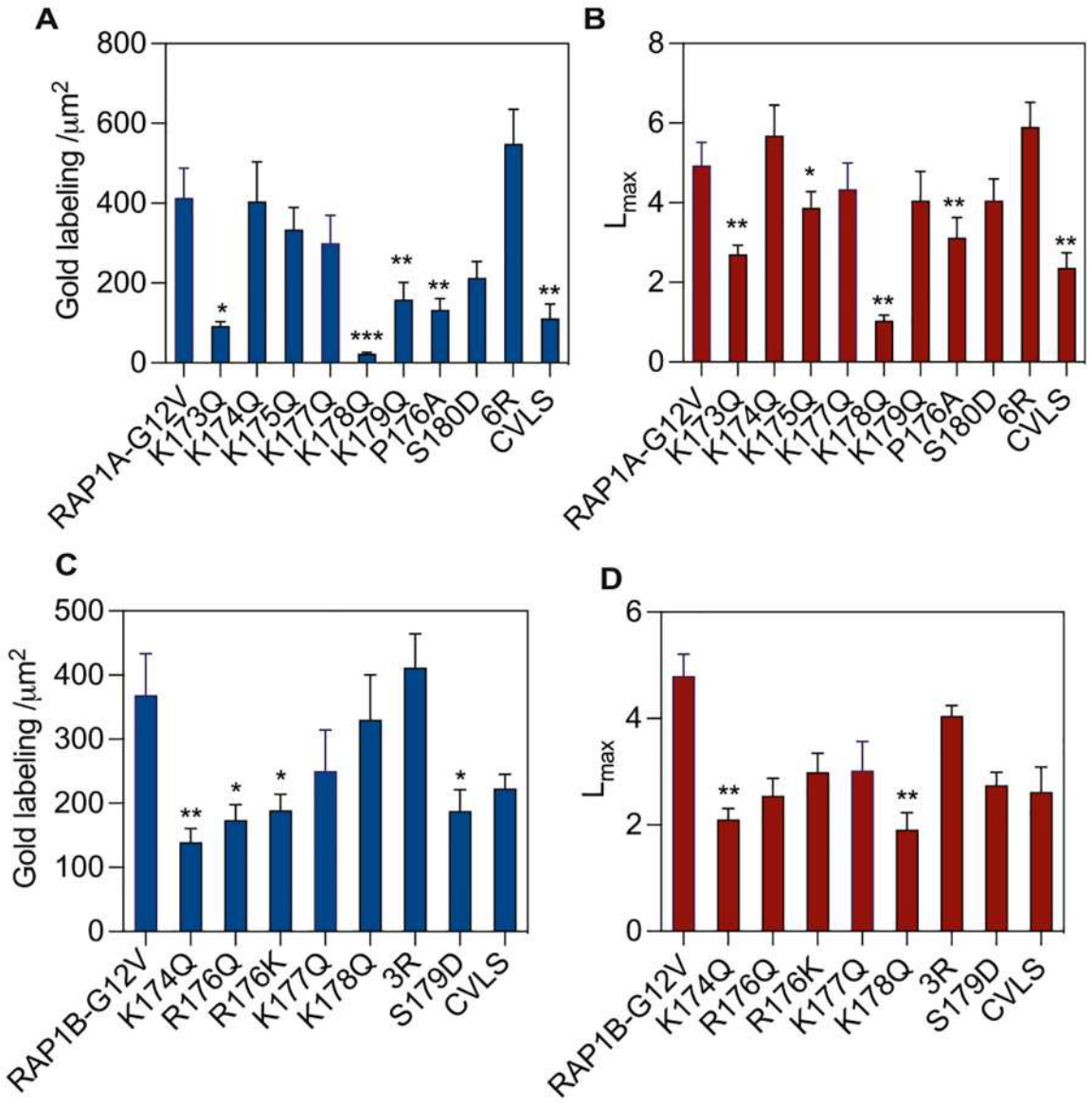

Figure 3.

RAP1 PBD mutants exhibit different PM binding affinities. (A–D) PM sheets of BHK cells expressing GFP-RAP1A or RAP1B anchor mutants were labeled with 4.5 nm gold-anti-GFP and analyzed by EM. PM localization was quantified as mean gold labeling intensity per 1 μm^2 and is shown as mean ± SEM (A,C), and the extent of nanoclustering is summarized as L_{max} (mean ± SEM, $n \geq 12$) (B,D). (A–D) Significant differences between L_{max} values for RAP1 PBD wild-type (RAP1-G12V) and each anchor mutants were evaluated in bootstrap tests (*$p < 0.05$, and **$p < 0.01$), and differences in gold labeling density were evaluated in two-tailed *t* tests (*$p < 0.05$, and **$p < 0.01$).

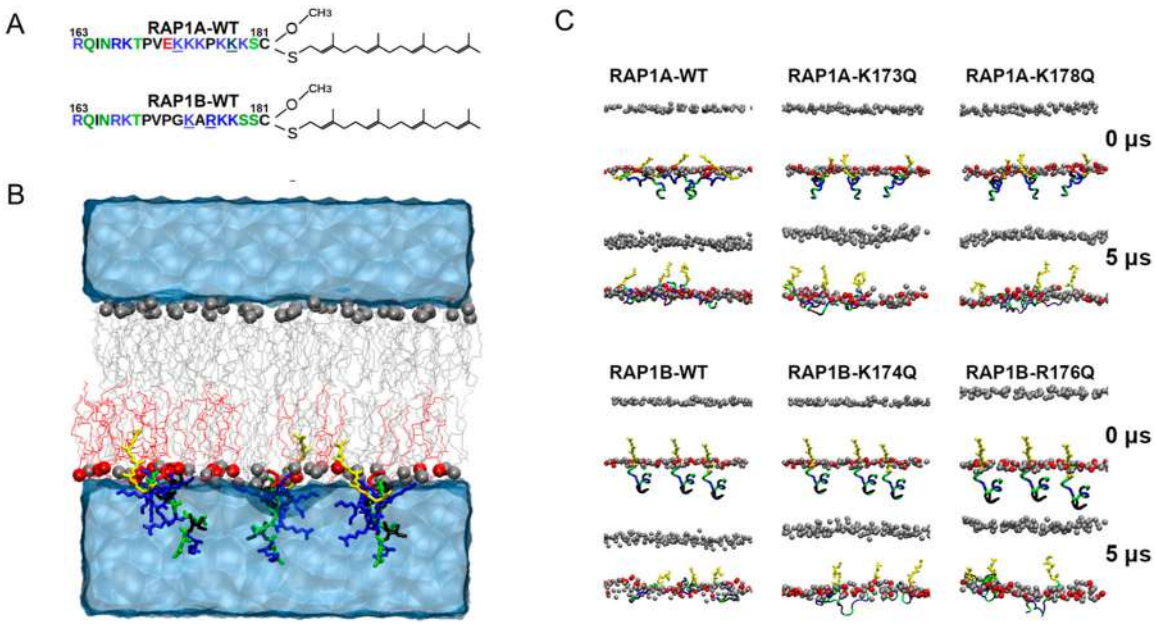

Figure 4.

Simulation setup and bilayer adsorption of RAP1A and RAP1B membrane anchor mutants. (A) Sequence of the RAP1A and RAP1B membrane anchors with basic residues in blue, acidic in red, polar in green, and hydrophobic residues in black. The underlined Lys or Arg residues were mutated to Gln, and the C-terminal Cys residue is carboxymethylated following geranylgeranylation. (B) Example of MD simulation setup, with three peptides embedded in the mixed-lipid leaflet of an asymmetric model membrane composed of POPC (gray) and POPS lipids (red). Lipid phosphorus atoms are shown in vdW spheres and the peptides (in this case RAP1A WT) in licorice colored as shown in panel A except for the prenylated Cys residue, which is in yellow. Water and ions are shown as a blue surface. (C) Snapshots at the start ($t = 0$ μs) and end ($t = 5$ μs) of the MD simulations of membrane-embedded wild-type and indicated mutant RAP1A and RAP1B membrane anchors, showing complete adsorption of the peptides on the bilayer surface at the end of the simulation. Only lipid phosphorus atoms, peptide backbone, and prenyl chains are shown colored as in panel B while the rest of the atoms are omitted for clarity.

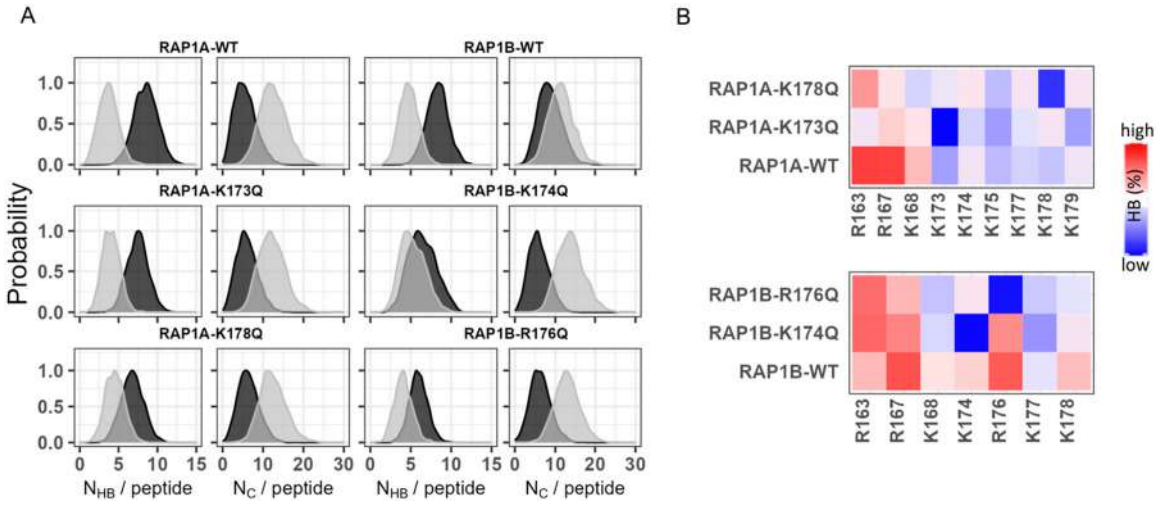

Figure 5.

Interactions of RAP1A and RAP1B with lipids. (A) Distribution of peptide-lipid HB (N_{HB}) and van der Waals (vdW) contacts (N_C) per peptide separately for POPC (gray) and POPS (black). HB was defined with a donor–acceptor distance cutoff of 3.1 Å and a donor-hydrogen-acceptor angle cutoff of 30° and included all polar and charged side chains and lipid headgroup oxygen atoms. N_C was computed using a carbon–carbon distance cutoff of 4 Å and included all nonpolar side-chain carbons (including the prenylated cysteines) and lipid acyl chain carbon atoms. (B) Heatmap of normalized HB frequency (HB) between the PBD Lys or Arg side chains with POPS headgroup oxygen atoms.